ELSEVIER

Contents lists available at ScienceDirect

Additive Manufacturing Letters

journal homepage: www.elsevier.com/locate/addlet



Mitigating keyhole pore formation by nanoparticles during laser powder bed fusion additive manufacturing



Minglei Qu^{a,b}, Qilin Guo^{a,b}, Luis I. Escano^a, Samuel J. Clark^c, Kamel Fezzaa^c, Lianyi Chen^{a,b,*}

- ^a Department of Mechanical Engineering, University of Wisconsin-Madison, Madison, WI 53706, United States
- b Department of Materials Science and Engineering, University of Wisconsin-Madison, Madison, WI 53706, United States
- ^cX-Ray Science Division, Argonne National Laboratory, Lemont, IL 60439, United States

ARTICLE INFO

Keywords: Keyhole pore Additive manufacturing Laser powder bed fusion Synchrotron x-ray imaging Nanoparticle

ABSTRACT

Keyhole pore formation is one of the most detrimental subsurface defects in the laser metal additive manufacturing process. However, effective ways to mitigate keyhole pore formation beyond tuning laser processing conditions during keyhole mode laser melting are still lacking. Here we report a novel approach to mitigate keyhole pore formation during laser powder bed fusion (LPBF) process by using stable nanoparticles. The critical keyhole depth for keyhole pore generation (i.e., the largest keyhole depth without keyhole pore formation) during LPBF of Al6061 increases from 246 μ m to 454 μ m (85% increase) after adding TiC nanoparticles. In-depth x-ray imaging studies and thermo-fluid dynamics simulation enable us to identify that two mechanisms work together to mitigate keyhole pore generation: (1) adding nanoparticles prevents the keyhole from collapsing by increasing the liquid viscosity to impede the protrusion development; (2) adding nanoparticles slows down the keyhole pore movement by increasing the liquid viscosity, resulting in the recapturing of the pore by the keyhole. We further demonstrate that adding TiC nanoparticles can also eliminate the keyhole fluctuation induced keyhole pore during LPBF of Al6061. Our research provides a potential way to mitigate keyhole pore formation for defect lean metal additive manufacturing.

1. Introduction

Laser metal additive manufacturing (AM, also known as 3D printing) is now widely used in aerospace, energy, medical and other industries due to its advantages of making complex and customized geometry, minimizing component quantity and processing steps, shortening lead time [1-7]. Laser powder bed fusion (LPBF) is one of the most popular laser metal AM technologies [5,8]. During LPBF process, a focused laser beam is used to selectively melt and fuse metal powders based on the computer-aided design model to create the part with desired shape [9,10]. As the high-energy laser beam interacts with the metal, the local temperature due to the laser heating can exceed the boiling temperature, causing material vaporization [11,12]. The recoil pressure induced by the vaporization pushes the liquid surface downwards to form a keyhole (or called vapor depression, or depression zone) [13-15]. Due to the dynamic change of the laser beam path and laser absorption within the keyhole, the temperature of the liquid surface around the keyhole changes significantly [16]. Consequently, the surface tension, recoil pressure and Marangoni convection, which are highly temperature dependent and are the major driving forces for keyhole dynamics, change significantly, resulting in severe fluctuation and, sometimes, collapse of the keyhole [14,17,18]. The pore generation due to keyhole collapse (i.e., keyhole pore) can get trapped by the solidification front and remains inside the printed part, which significantly degrades mechanical properties (e.g., fatigue life) [19,20].

Significant efforts have been made to investigate the keyhole pore formation in the laser metal AM and laser welding process [21–27], and most reported studies for mitigating keyhole pores rely on reducing the laser energy input (i.e., increasing the laser scan speed or decreasing the laser power) [28–33] and pulsing or oscillating the laser beam [34–36]. Another reported method to avoid or control the keyhole pore formation during laser melting is by reducing the ambient pressure [37,38]. However, the decrease of the ambient pressure may prevent powders from entering melt pool during LPBF process, compromising the final part quality [39,40]. So far, effective and feasible ways to mitigate the keyhole pore formation beyond tuning laser processing conditions are still lacking. Therefore, to avoid the keyhole pore formation, the laser processing parameter is limited to a small window (i.e., the keyhole depth should be smaller than a critical value) [14], which makes LPBF process very susceptible to the energy input disturbance (which often

^{*} Corresponding author at: Department of Mechanical Engineering, University of Wisconsin-Madison, Madison, WI 53706, United States. E-mail address: lianyi.chen@wisc.edu (L. Chen).

occurs in the LPBF process, such as the increase of local energy input at laser turning point [27], varied substrate temperature [41]) to generate keyhole pores. The critical keyhole depth also significantly hinders the process efficiency improvement by limiting the further increase in absorption and the use of larger powder layer thickness [42].

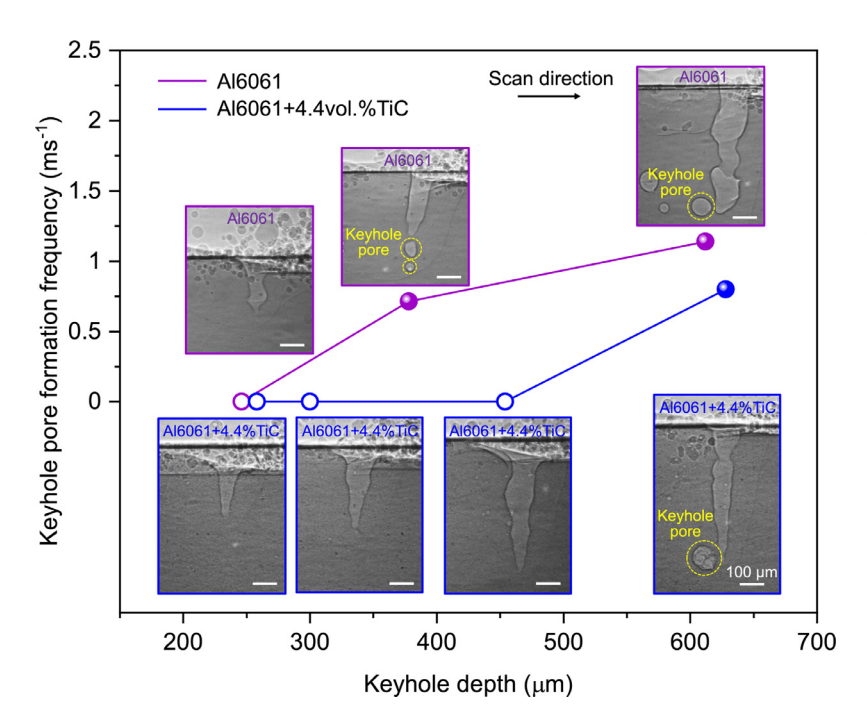
Adding nanoparticles can alter material properties [43–45]. Our previous study shows that the nanoparticle-induced material property change can lead to the elimination of the liquid breakup from melt pool by stabilizing the keyhole fluctuation [45]. However, the effects of nanoparticles on the keyhole pore formation, keyhole collapsing dynamics and keyhole pore evolution have not been studied and are still unclear.

Here, we report using nanoparticles to mitigate keyhole pore generation in LPBF process. The critical keyhole depth for keyhole pore generation (i.e., the largest keyhole depth without keyhole pore formation) during LPBF of Al6061 increases from 246 µm to 454 µm (85% increase) after adding TiC nanoparticles. In-depth x-ray imaging studies and thermo-fluid dynamics simulation enable us to identify that two mechanisms work together to mitigate keyhole pore generation: (1) adding nanoparticles prevents the keyhole from collapsing by increasing the liquid viscosity to impede the protrusion development; (2) adding nanoparticles slows down the keyhole pore movement by increasing the liquid viscosity, resulting in the recapturing of pore by the keyhole. We further demonstrate that adding TiC nanoparticles can also eliminate the keyhole fluctuation induced keyhole pore during LPBF of Al6061. Our research provides a potential way to mitigate keyhole pore formation for defect lean metal additive manufacturing.

2. Material and methods

2.1. Materials

The Al6061 powders (D10: 17 μ m, D50: 34 μ m, D90: 60 μ m) were purchased from the Valimet (USA). The Al6061 substrate was cut from the commercial Al6061 plate (T6511, Mcmaster-Carr, USA). The Al6061+4.4 vol.%TiC powders were prepared by planetary ball milling of the Al6061 powders and TiC nanoparticles (83 nm, SSnano, USA). The Al6061+4.4 vol.%TiC substrate was cut from the as-printed Al6061+4.4 vol.%TiC part.



2.2. In-situ high-speed x-ray imaging experiment

The *in-situ* x-ray imaging experiment was performed (at the beamline 32-ID-B, Advanced Photon Source, Argonne National Laboratory) to study the effects of nanoparticles on the keyhole pore formation during LPBF process of Al6061 and Al6061+4.4 vol.%TiC. During experiments, a focused laser beam (1070 nm wavelength, continuous-wave, single mode, D4 σ of 90 μ m) generated by an ytterbium fiber laser (YLR-500-AC, IPG Photonics, USA) was used to perform LPBF experiments. The laser path was controlled by a galvo scan head (intelliSCANde 30, SCANLAB GmbH, Germany). During laser melting, the x-ray simultaneously penetrated through the laser scanning area. The transmitted x-ray signal carrying the information of the keyhole and keyhole pore dynamics was converted by a scintillator into a visible light, which was then recorded by a high-speed camera with a frame rate of 50 kHz. The resolution of the x-ray image is 1.93 μ m per pixel.

2.3. Computational thermo-fluid dynamics simulation

To discern the underlying mechanisms for the nanoparticle-induced keyhole pore mitigation, we performed the computational thermo-fluid dynamics simulation using the Flow-3D software (FLOW-3D 12.0, Flow Sciences, USA). To trace the keyhole dynamics more accurately, the multiple reflection inside the keyhole was considered. The Fresnel equation was utilized to calculate the absorption/reflection at each laser incidence at the keyhole-liquid interface. The driving forces, including the recoil pressure, thermocapillary force, gravity force, and buoyance force, were considered in the model. The mesh size is 4 μm . Details about the model setup, governing equation and material properties for Al6061 can be found in reference [45].

3. Results and discussion

3.1. Mitigating keyhole pore formation by nanoparticles

To study the effects of nanoparticles on the keyhole pore formation during LPBF process, we performed the *in-situ* high-speed x-ray imaging experiment to characterize the keyhole pore formation during LPBF of Al6061 and Al6061+4.4 vol.%TiC under different laser powers (to generate different keyhole depths) and 0.2 m/s scan speed. The results

Fig. 1. X-ray images showing keyhole depth threshold for generating keyhole pore during LPBF of Al6061 and Al6061+4.4 vol.%TiC. The keyhole pore formation frequency in y-axis is defined as the rate at which the keyhole pore is formed in the printed sample (based on the x-ray images). The open circle indicates the condition without keyhole pore generation. The solid circle indicates the condition with keyhole pore generation. Adding nanoparticles significantly increases the keyhole depth threshold for generating the keyhole pore. The laser scan direction for all the x-ray images is the same and indicated by the dark arrow. All the scale bars represent 100 μm.

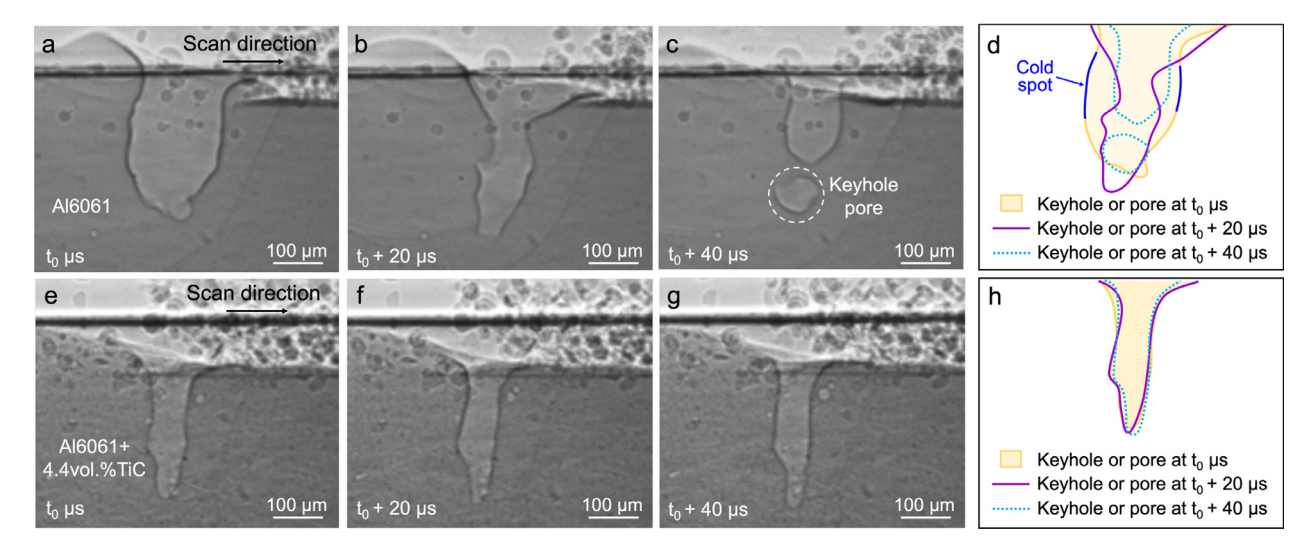


Fig. 2. Nanoparticle-enabled prevention of keyhole collapse. a-c, X-ray images showing that the keyhole collapse results in the generation of keyhole pore during LPBF of Al6061. White dashed circle indicates the keyhole pore. a, At t_0 μs, the keyhole expands with the width (174 μm) much larger than the laser beam size (90 μm). b, At t_0 + 20 μs, the liquid starts to close the keyhole driven by the surface tension. c, At t_0 + 40 μs, the keyhole collapses, and a keyhole pore is generated. d, Contours showing the dynamics of the keyhole and pore during LPBF of Al6061. e-g, X-ray images showing that the keyhole keeps open without generating the keyhole pore during LPBF of Al6061+4.4 vol.%TiC. h, Contours showing the dynamics of the keyhole and pore during LPBF of Al6061+4.4 vol.%TiC. The laser scan direction is indicated by the dark arrows.

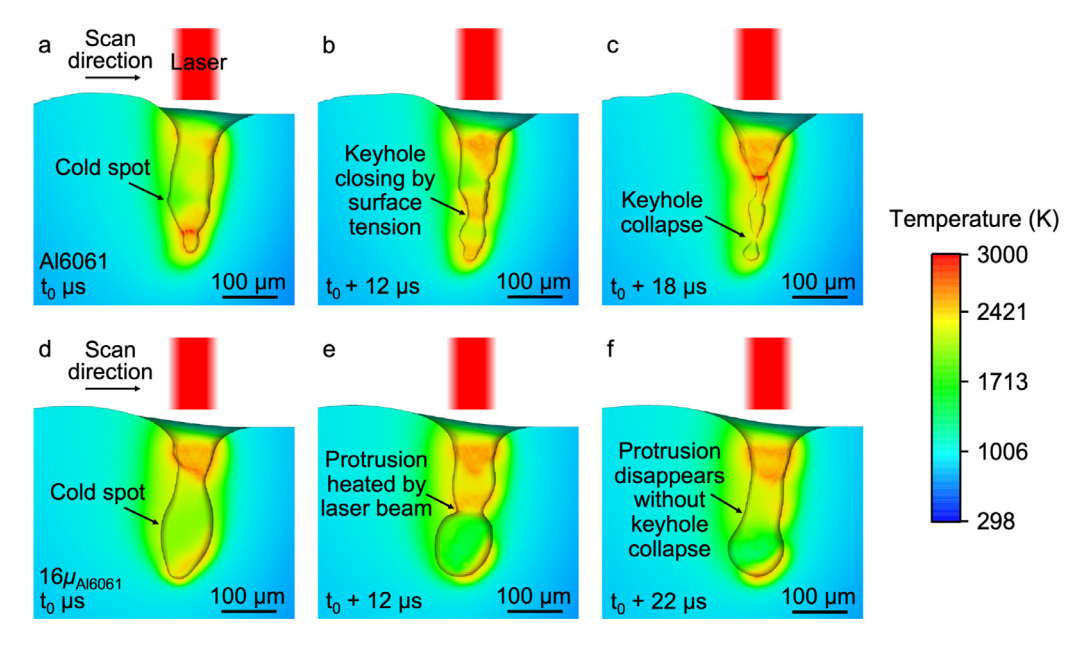


Fig. 3. Simulation results elucidating the mechanisms of nanoparticle-enabled prevention of keyhole collapse. a-c, Simulation results showing the keyhole collapse-induced pore generation during laser melting of Al6061. a, At t_0 μ s, a cold spot is generated at liquid surface. b, At $t_0 + 12$ μ s, the liquid starts to close the keyhole driven by the surface tension. c, At $t_0 + 18$ μ s, the keyhole collapses, and a pore is generated. d-f, Simulation results showing that increasing viscosity (16 times as high as that of Al6061) prevents keyhole from collapsing. d, At t_0 μ s, a cold spot is generated at liquid surface. e, At $t_0 + 12$ μ s, the liquid starts to close the keyhole, generating a protrusion at liquid surface. f, At $t_0 + 22$ μ s, the slowly developing protrusion (due to high liquid viscosity) allows the laser to heat it to high temperature, and the resulting recoil pressure pushes the protrusion back to the liquid without keyhole collapse. Based on the measurement results that the viscosity of Al6061+4.4 vol.%TiC is 16 times as high as that of Al6061, 16 times viscosity is used in the simulation d-f. In the simulation (a-f), the laser power is 416 W, the scan speed is 0.2 m/s.

show that for both Al6061 and Al6061+4.4 vol.%TiC, the keyhole pore is generated after the keyhole depth increases to a certain threshold [14]. For Al6061, the maximum keyhole depth without generating the keyhole pore is 246 μ m. In contrast, for Al6061+4.4 vol.%TiC, we observe a 85% increase of this critical keyhole depth from 246 μ m to 454 μ m without generating the keyhole pore (Fig. 1). This suggests that adding nanoparticles can significantly enlarge the processing window without generating the keyhole pore. It should be noted that, although adding TiC nanoparticles can eliminate the keyhole pore formation un-

der certain keyhole depth range, we still observe keyhole pore generation when the keyhole depth is extremely large (i.e. 628 $\mu m)$ during LPBF of Al6061+4.4 vol.%TiC (Fig. 1).

3.2. Mechanisms of nanoparticle-induced mitigation of keyhole pore

To realize the underlying mechanism for the nanoparticle-induced keyhole pore mitigation, we performed in-depth *in-situ* x-ray imaging studies and computational thermo-fluid dynamics simulation. We iden-

tified that two mechanisms work together to mitigate the keyhole pore formation: (1) nanoparticles prevent the keyhole from collapsing; (2) nanoparticles impede the keyhole pore movement, allowing the keyhole pore to be recaptured by the keyhole.

The first mechanism we identified is that adding nanoparticles can prevent the keyhole from collapsing. To study the effects of nanoparticles on the keyhole collapsing behavior, we performed in-depth *in-situ*

x-ray imaging experiments to characterize the keyhole collapsing dynamics during LPBF of Al6061 and Al6061+4.4 vol.%TiC. For Al6061, we observe that the keyhole collapsing event often starts with an expanded keyhole (Fig. 2a, the keyhole width is 174 μm compared with the laser beam size of 90 μm), resulting in the decrease of temperature for liquid surface far away from the laser beam. The temperature decrease further causes the increase of the surface tension and decrease of

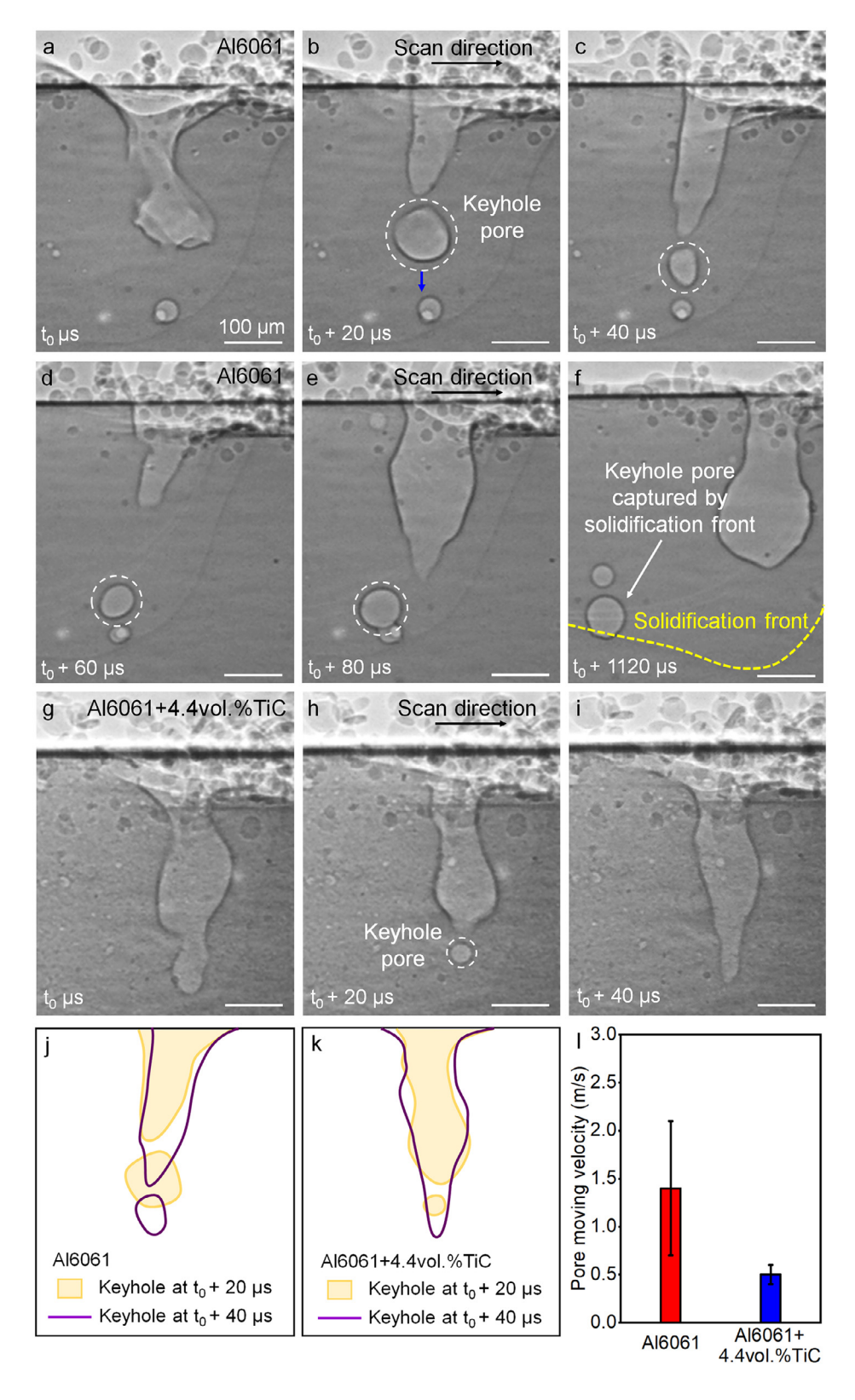


Fig. 4. Nanoparticle-enabled controlling of keyhole pore movement. a-f, X-ray images showing that the generated keyhole pore is pushed away from keyhole and later captured by the solidification front during LPBF of Al6061. White dashed circle indicates the keyhole pore. Blue arrow indicates the keyhole pore moving direction. g-i, X-ray images showing that the generated keyhole pore is recaptured by the keyhole during LPBF of Al6061+4.4 vol.%TiC. j, k, Contours showing the dynamics of the keyhole and pore during LPBF of Al6061 (j) and Al6061+4.4 vol.%TiC (k). l, The average keyhole pore moving velocity during LPBF of Al6061 and Al6061+4.4 vol.%TiC. In (a-i), the scale bars represent 100 μm.

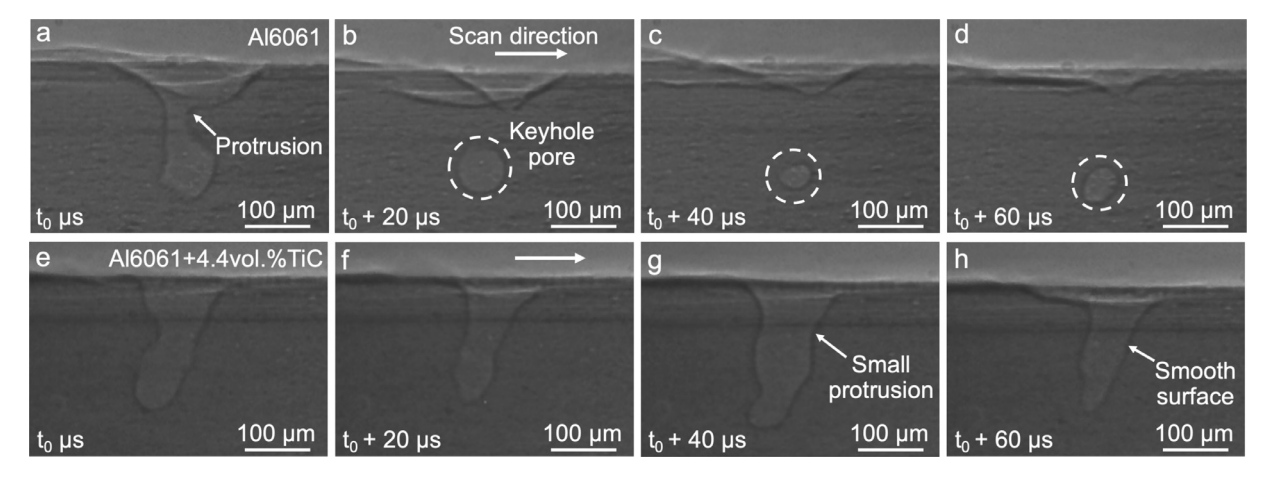


Fig. 5. Nanoparticle-enabled elimination of keyhole fluctuation induced keyhole pore. a–d, X-ray images showing that the protrusion at the keyhole front wall causes the sudden decrease of the keyhole depth, resulting in the generation of keyhole pore during LPBF of Al6061. Keyhole pore is indicated by the white dashed circle. e–h, X-ray images showing the smooth keyhole front wall without any keyhole pore generation during LPBF of Al6061+4.4 vol.%TiC.

the recoil pressure. Therefore, the liquid movement driven by the surface tension (moving towards the center of the keyhole) closes the keyhole in the middle height, resulting in the generation of keyhole pore (Fig. 2b–d). For Al6061, the keyhole collapses very frequently (collapses every 0.4 ms at the keyhole depth of 378 µm). In contrast, the keyhole collapsing frequency significantly decreases (collapses every 2 ms at the keyhole depth of 454 µm, the frequency decreases 78% compared with Al6061) during LPBF of Al6061+4.4 vol.%TiC. For most of the time, the keyhole keeps open without collapsing (Fig. 2e–h). This suggests that adding nanoparticles can prevent the keyhole from collapsing.

We attributed the nanoparticle-induced prevention of keyhole collapsing to the increased viscosity by nanoparticles (i.e., the solid TiC nanoparticles in the liquid Al6061, as reported in [45], increase the viscosity of the liquid Al6061). To confirm this, we performed the thermophysical stimulation to study the effect of nanoparticle-induced increase of viscosity (the viscosity of Al6061+4.4 vol.%TiC is 16 times as high as that of Al6061, detailed in [45]) on the keyhole collapsing dynamics. Specifically, we performed two simulations. The reference simulation used all the material properties from Al6061 [45]. In another simulation, we increased the viscosity to 16 times as high as that of Al6061 while other properties are the same as that of Al6061. During the simulation of Al6061, we observe that when a cold liquid spot (i.e., the relatively colder area on the liquid surface caused by uneven heating of the laser beam) is generated (Fig. 3a), the liquid starts to close the keyhole driven by the surface tension force (Fig. 3b), and finally the keyhole collapses with a keyhole pore generated (Fig. 3c). The horizontal velocity of the liquid movement (to close the keyhole) is 4.3 m/s. After increasing the viscosity to 16 times as high as that of Al6061, we still observe that liquid tends to close the keyhole at certain moment (Fig. 3d, e). However, the horizontal velocity of liquid movement (to close the keyhole) after increasing viscosity decreases 79% from 4.3 m/s to 0.9 m/s, indicating a much longer time is required for the liquid to close the keyhole. During this time, the laser beam can heat the protrusion (generated during the closing of the keyhole, indicated in Fig. 3e) to a very high temperature. As a result, the recoil pressure impinged on the protrusion overcomes the surface tension to push the protrusion back into the liquid and, thereby, prevent the keyhole from collapsing (Fig. 3f). This suggests that adding nanoparticles can prevent the keyhole from collapsing by increasing the

Another mechanism for the nanoparticle-induced keyhole pore mitigation we identified is that even though sometimes the keyhole collapses during LPBF of Al6061+4.4 vol.%TiC, the generated keyhole pore can be easily recaptured by the keyhole instead of being pushed away by the strong melt flow and staying in the melt pool. During LPBF of Al6061,

we observe from x-ray images that, after the keyhole collapses, the pore is pushed away by the strong melt flow induced by the recoil pressure (the pore movement may also be driven by the vapor shear force and Marangoni force induced melt flow or inherent melt flow pattern [46]), then is captured by the solidification front and remains in the solidified part (Fig. 4a-f). In contrast, during LPBF of Al6061+4.4 vol.%TiC, when the keyhole occasionally collapses (Fig. 4h), the pore is immediately recaptured by the keyhole at the next frame to eliminate the pore (Fig. 4i). This suggests that the pores generated due to the keyhole collapse do not always survive in the final part. Whether the pore can survive depends on its location and moving speed with respect to the keyhole (i.e., whether the pore can be later recaptured by the keyhole). Adding nanoparticles can increase the liquid viscosity to impede the pore movement (i.e., movement away from keyhole), so that the keyhole pore can later be recaptured by the keyhole to eliminate the keyhole pore. We also quantified the keyhole pore moving velocity after the keyhole collapses. The moving velocity of the pore was measured by dividing its displacement by the moving time. The displacement of the pore was calculated through its 2-D coordinate change (i.e., the projection in the longitudinal cross section plane) from one frame to the next frame in the x-ray imaging experiment. The moving time is the time interval between two frames, which is determined by the recording frame rate (50 kHz). The average keyhole pore moving velocity during LPBF of Al6061 is 1.4 ± 0.7 m/s, compared with the average moving velocity of 0.5 ± 0.1 m/s for the Al6061+4.4 vol.%TiC (Fig. 4l). This further validates our proposed mechanism.

3.3. Elimination of keyhole fluctuation induced pore

We have demonstrated that nanoparticles can mitigate the keyhole pore caused by the keyhole collapse (i.e., a sudden decrease of the keyhole width results in the separation of pore from the keyhole bottom). Previous research reported that the keyhole pore can also be generated in a shallow keyhole due to the keyhole fluctuation (i.e., keyhole depth suddenly decreases and almost disappears) [22]. Here we observe the similar phenomenon that, during the LPBF of Al6061, the depth of the keyhole suddenly decreases from 213 μm to 55 μm , accompanied by the generation of the keyhole pore (Fig. 5a–d). The sudden decrease of the keyhole depth can be attributed to the decrease of the recoil pressure. During LPBF of Al6061, we observe that before the keyhole depth decreases, a large tongue-like protrusion forms on the keyhole front wall (Fig. 5a), which may significantly decrease the absorption and recoil pressure impinged on the liquid beneath the protrusion, resulting in a sudden decrease of the keyhole depth. In contrast, during LPBF of

Al6061+4.4 vol.%TiC, we observe that only small dome-like protrusions (indicated in Fig. 5g) are formed without significantly blocking the laser beam. This is because the high viscosity of liquid Al6061+4.4 vol.%TiC can slow down the protrusion development. Before the small protrusion further develops into a large tongue-shape protrusion, the laser beam has enough time to heat up the protrusion surface so that the recoil pressure can push the protrusion back. The relatively smooth keyhole front surface without large protrusion during LPBF of Al6061+4.4 vol.%TiC leads to a more uniform heating of the liquid surface from the keyhole top to the bottom, so that the recoil pressure can support the keyhole shape without sudden decease of the keyhole depth or generating the keyhole pore (Fig. 5e–h). This suggests that adding nanoparticles can also eliminate the keyhole fluctuation induced keyhole front wall.

4. Conclusion

In this work, we report a novel approach to mitigate the keyhole pore formation during LPBF process by using nanoparticles. We also identify the underlying mechanisms by performing the in-depth *in-situ* x-ray imaging experiment and computational thermo-fluid dynamics simulation. The major conclusions are as follows:

- (1) Nanoparticles can significantly increase the critical keyhole depth for keyhole pore generation (i.e., the largest keyhole depth without keyhole pore formation) and expand the process window without keyhole pore generation during LPBF process. After adding 4.4 vol.% TiC nanoparticles into Al6061, the critical keyhole depth for keyhole pore generation increases 85% from 246 μm to 454 μm .
- (2) Two mechanisms for nanoparticle-induced keyhole pore mitigation were identified. First, adding nanoparticle can prevent the keyhole from collapsing by slowing down the protrusion development. Thus, the laser has more time to heat the protrusion to higher temperature, and the resulting recoil pressure pushes the protrusion back to the liquid without keyhole collapse. Second, adding nanoparticles slows down the keyhole pore movement by increasing the viscosity, resulting in the recapturing of pore by the keyhole. The average moving velocity of the keyhole pore during the LPBF of Al6061 is 1.4 ± 0.7 m/s, compared with the average velocity of 0.5 ± 0.1 m/s for the Al6061+4.4 vol.%TiC.
- (3) Adding nanoparticles can also eliminate the keyhole fluctuation induced keyhole pore. This is because adding nanoparticles can slow down the protrusion development at the keyhole front wall to allow enough laser heating of the protrusion so that the recoil pressure can push back the protrusion without further developing into a large one. The resulting smooth front wall without large protrusion leads to a more uniform laser heating of liquid surface. Therefore, the recoil pressure can support the keyhole shape without sudden decease of keyhole depth or generating the keyhole pore.

The method and mechanisms of using nanoparticles to mitigate the keyhole pore formation reported here provide a potential way to mitigate the keyhole pore formation for defect lean metal AM. The concept of using nanoparticles to increase the critical keyhole depth for keyhole pore generation also has implications for laser welding.

Declaration of Competing Interest

The authors declare that they have no known competing financial interests or personal relationships that could have appeared to influence the work reported in this paper.

Acknowledgements

This work is supported by US National Science Foundation and University of Wisconsin-Madison Startup Fund. This research used resources of the Advanced Photon Source, a U.S. Department of Energy (DOE) Office of Science User Facility operated for the DOE Office of Science by Argonne National Laboratory under Contract No. DE-AC02-06CH11357.

References

- T. DebRoy, T. Mukherjee, J.O. Milewski, J.W. Elmer, B. Ribic, J.J. Blecher, W. Zhang, Scientific, technological and economic issues in metal printing and their solutions, Nat. Mater. 18 (2019) 1026–1032. doi:10.1038/s41563-019-0408-2.
- [2] T. DebRoy, T. Mukherjee, H.L. Wei, J.W. Elmer, J.O. Milewski, Metallurgy, mechanistic models and machine learning in metal printing, Nat. Rev. Mater. 6 (2021) 48–68. doi:10.1038/s41578-020-00236-1.
- [3] T. Wohlers, Wohlers Report 2020: 3D Printing and Additive Manufacturing Global State of the Industry, Wohlers Associates, Inc., 2020.
- [4] C. Han, Q. Fang, Y. Shi, S.B. Tor, C.K. Chua, K. Zhou, Recent advances on high-entropy alloys for 3D printing, Adv. Mater. 32 (2020) 1903855, doi:10.1002/adma.201903855.
- [5] W.E. King, A.T. Anderson, R.M. Ferencz, N.E. Hodge, C. Kamath, S.A. Khairallah, A.M. Rubenchik, Laser powder bed fusion additive manufacturing of metals; physics, computational, and materials challenges, Appl. Phys. Rev. 2 (2015) 041304, doi:10.1063/1.4937809.
- [6] M.S. Pham, C. Liu, I. Todd, J. Lertthanasarn, Damage-tolerant architected materials inspired by crystal microstructure, Nature 565 (2019) 305–311, doi:10.1038/s41586-018-0850-3.
- [7] B. Hanks, J. Berthel, M. Frecker, T.W. Simpson, Mechanical properties of additively manufactured metal lattice structures: data review and design interface, Addit. Manuf. 35 (2020) 101301, doi:10.1016/j.addma.2020.101301.
- [8] Y. Li, K. Zhou, P. Tan, S.B. Tor, C.K. Chua, K.F. Leong, Modeling temperature and residual stress fields in selective laser melting, Int. J. Mech. Sci. 136 (2018) 24–35, doi:10.1016/j.ijmecsci.2017.12.001.
- [9] W.E. King, H.D. Barth, V.M. Castillo, G.F. Gallegos, J.W. Gibbs, D.E. Hahn, C. Kamath, A.M. Rubenchik, Observation of keyhole-mode laser melting in laser powder-bed fusion additive manufacturing, J. Mater. Process. Technol. 214 (2014) 2915–2925, doi:10.1016/j.jmatprotec.2014.06.005.
- [10] C.L.A. Leung, S. Marussi, R.C. Atwood, M. Towrie, P.J. Withers, P.D. Lee, *In situ x-ray* imaging of defect and molten pool dynamics in laser additive manufacturing, Nat. Commun. 9 (2018) 1355, doi:10.1038/s41467-018-03734-7.
- [11] L. Wang, Y. Zhang, W. Yan, Evaporation model for keyhole dynamics during additive manufacturing of metal, Phys. Rev. Appl. 14 (2020) 064039, doi:10.1103/PhysRevApplied.14.064039.
- [12] A.A. Martin, N.P. Calta, J.A. Hammons, S.A. Khairallah, M.H. Nielsen, R.M. Shuttlesworth, N. Sinclair, M.J. Matthews, J.R. Jeffries, T.M. Willey, J.R.I. Lee, Ultrafast dynamics of laser-metal interactions in additive manufacturing alloys captured by in situ X-ray imaging, Mater. Today Adv. 1 (2019) 100002, doi:10.1016/j.mtadv.2019.01.001.
- [13] Y. Chen, S.J. Clark, C.L.A. Leung, L. Sinclair, S. Marussi, M.P. Olbinado, E. Boller, A. Rack, I. Todd, P.D. Lee, *In-situ* synchrotron imaging of keyhole mode multi-layer laser powder bed fusion additive manufacturing, Appl. Mater. Today 20 (2020) 100650, doi:10.1016/j.apmt.2020.100650.
- [14] C. Zhao, N.D. Parab, X. Li, K. Fezzaa, W. Tan, A.D. Rollett, T. Sun, Critical instability at moving keyhole tip generates porosity in laser melting, Science 370 (2020) 1080– 1086, doi:10.1126/science.abd1587.
- [15] R. Cunningham, C. Zhao, N. Parab, C. Kantzos, J. Pauza, K. Fezzaa, T. Sun, A.D. Rollett, Keyhole threshold and morphology in laser melting revealed by ultrahigh-speed x-ray imaging, Science 363 (2019) 849–852, doi:10.1126/science.aav4687.
- [16] N. Kouraytem, X. Li, R. Cunningham, C. Zhao, N. Parab, T. Sun, A.D. Rollett, A.D. Spear, W. Tan, Effect of laser-matter interaction on molten pool flow and keyhole dynamics, Phys. Rev. Appl. 11 (2019) 064054, doi:10.1103/PhysRevApplied 11 064054.
- [17] A. Matsunawa, J.-D. Kim, N. Seto, M. Mizutani, S. Katayama, Dynamics of keyhole and molten pool in laser welding, J. Laser Appl. 10 (1998) 247–254, doi:10.2351/1.521858.
- [18] S. Pang, L. Chen, J. Zhou, Y. Yin, T. Chen, A three-dimensional sharp interface model for self-consistent keyhole and weld pool dynamics in deep penetration laser welding, J. Phys. D Appl. Phys. 44 (2011) 025301, doi:10.1088/0022-3727/44/2/025301.
- [19] S. Tammas-Williams, P.J. Withers, I. Todd, P.B. Prangnell, The influence of porosity on fatigue crack initiation in additively manufactured titanium components, Sci. Rep. 7 (2017) 7308, doi:10.1038/s41598-017-06504-5.
- [20] E.W. Jost, J.C. Miers, A. Robbins, D.G. Moore, C. Saldana, Effects of spatial energy distribution-induced porosity on mechanical properties of laser powder bed fusion 316 L stainless steel, Addit. Manuf. 39 (2021) 101875, doi:10.1016/j.addma.2021.101875.
- [21] S.A. Khairallah, A.T. Anderson, A. Rubenchik, W.E. King, Laser powder-bed fusion additive manufacturing: physics of complex melt flow and formation mechanisms of pores, spatter, and denudation zones, Acta Mater. 108 (2016) 36–45, doi:10.1016/j.actamat.2016.02.014.
- [22] S.M.H. Hojjatzadeh, N.D. Parab, Q. Guo, M. Qu, L. Xiong, C. Zhao, L.I. Escano, K. Fezzaa, W. Everhart, T. Sun, L. Chen, Direct observation of pore formation mechanisms during LPBF additive manufacturing process and high energy density laser welding, Int. J. Mach. Tools Manuf. 153 (2020) 103555, doi:10.1016/j.ijmachtools.2020.103555.
- [23] Y. Huang, T.G. Fleming, S.J. Clark, S. Marussi, K. Fezzaa, J. Thiyagalingam, C.L.A. Leung, P.D. Lee, Keyhole fluctuation and pore formation mechanisms during laser powder bed fusion additive manufacturing, Nat. Commun. 13 (2022) 1170, doi:10.1038/s41467-022-28694-x.
- [24] W. Tan, Y.C. Shin, Analysis of multi-phase interaction and its effects on keyhole dynamics with a multi-physics numerical model, J. Phys. D Appl. Phys. 47 (2014) 345501, doi:10.1088/0022-3727/47/34/345501.

- [25] S.A. Khairallah, A.A. Martin, J.R.I. Lee, G. Guss, N.P. Calta, J.A. Hammons, M.H. Nielsen, K. Chaput, E. Schwalbach, M.N. Shah, M.G. Chapman, T.M. Willey, A.M. Rubenchik, A.T. Anderson, Y. Morris Wang, M.J. Matthews, W.E. King, Controlling interdependent meso-nanosecond dynamics and defect generation in metal 3D printing, Science 368 (2020) 660–665, doi:10.1126/science.aay7830.
- [26] M. Bayat, A. Thanki, S. Mohanty, A. Witvrouw, S. Yang, J. Thorborg, N.S. Tiedje, J.H. Hattel, Keyhole-induced porosities in laser-based powder bed fusion (L-PBF) of Ti₆Al₄V: high-fidelity modelling and experimental validation, Addit. Manuf. 30 (2019) 100835, doi:10.1016/j.addma.2019.100835.
- [27] A.A. Martin, N.P. Calta, S.A. Khairallah, J. Wang, P.J. Depond, A.Y. Fong, V. Thampy, G.M. Guss, A.M. Kiss, K.H. Stone, C.J. Tassone, J. Nelson Weker, M.F. Toney, T. van Buuren, M.J. Matthews, Dynamics of pore formation during laser powder bed fusion additive manufacturing, Nat. Commun. 10 (2019) 1987, doi:10.1038/s41467-019-10009-2.
- [28] S. Shrestha, K. Chou, Formation of keyhole and lack of fusion pores during the laser powder bed fusion process, Manuf. Lett. 32 (2022) 19–23, doi:10.1016/j.mfglet.2022.01.005.
- [29] W. Wang, J. Ning, S.Y. Liang, Analytical prediction of keyhole porosity in laser powder bed fusion, Int. J. Adv. Manuf. Technol. 119 (2022) 6995–7002, doi:10.1007/s00170-021-08276-9
- [30] R. Cunningham, S.P. Narra, C. Montgomery, J. Beuth, A.D. Rollett, Synchrotron-based x-ray microtomography characterization of the effect of processing variables on porosity formation in laser power-bed additive manufacturing of Ti-6Al-4V, JOM 69 (2017) 479–484, doi:10.1007/s11837-016-2234-1.
- [31] A. du Plessis, Effects of process parameters on porosity in laser powder bed fusion revealed by X-ray tomography, Addit. Manuf. 30 (2019) 100871, doi:10.1016/j.addma.2019.100871.
- [32] S. Shrestha, T. Starr, K. Chou, A study of keyhole porosity in selective laser melting: single-track scanning with micro-CT analysis, J. Manuf. Sci. Eng. Trans. ASME 141 (2019) 071004, doi:10.1115/1.4043622.
- [33] Z. Gan, O.L. Kafka, N. Parab, C. Zhao, L. Fang, O. Heinonen, T. Sun, W.K. Liu, Universal scaling laws of keyhole stability and porosity in 3D printing of metals, Nat. Commun. 12 (2021) 2379, doi:10.1038/s41467-021-22704-0.
- [34] J. Zhou, H.L. Tsai, Porosity formation and prevention in pulsed laser welding, J. Heat Transf. 129 (2007) 1014–1024, doi:10.1115/1.2724846.
- [35] Z. Wang, J.P. Oliveira, Z. Zeng, X. Bu, B. Peng, X. Shao, Laser beam oscillating welding of 5A06 aluminum alloys: microstructure, porosity and mechanical properties, Opt. Laser Technol. 111 (2019) 58–65. doi:10.1016/j.optlastec.2018.09.036.

- [36] W. Ke, X. Bu, J.P. Oliveira, W.G. Xu, Z. Wang, Z. Zeng, Modeling and numerical study of keyhole-induced porosity formation in laser beam oscillating welding of 5A06 aluminum alloy, Opt. Laser Technol. 133 (2021) 106540, doi:10.1016/j.optlastec.2020.106540.
- [37] L. Wang, Y. Zhang, H.Y. Chia, W. Yan, Mechanism of keyhole pore formation in metal additive manufacturing, NPJ Comput. Mater. 8 (2022) 22, doi:10.1038/s41524-022-00699-6.
- [38] P. Tan, R. Kiran, K. Zhou, Effects of sub-atmospheric pressure on keyhole dynamics and porosity in products fabricated by selective laser melting, J. Manuf. Process. 64 (2021) 816–827, doi:10.1016/j.jmapro.2021.01.058.
- [39] Q. Guo, C. Zhao, L.I. Escano, Z. Young, L. Xiong, K. Fezzaa, W. Everhart, B. Brown, T. Sun, L. Chen, Transient dynamics of powder spattering in laser powder bed fusion additive manufacturing process revealed by in-situ high-speed high-energy x-ray imaging, Acta Mater. 151 (2018) 169–180, doi:10.1016/j.actamat.2018.03.036.
- [40] P. Bidare, I. Bitharas, R.M. Ward, M.M. Attallah, A.J. Moore, Laser powder bed fusion at sub-atmospheric pressures, Int. J. Mach. Tools Manuf. 130–131 (2018) 65–72, doi:10.1016/j.ijmachtools.2018.03.007.
- [41] P. Kürnsteiner, M.B. Wilms, A. Weisheit, B. Gault, E.A. Jägle, D. Raabe, Highstrength damascus steel by additive manufacturing, Nature 582 (2020) 515–519, doi:10.1038/s41586-020-2409-3.
- [42] V. Matilainen, H. Piili, A. Salminen, T. Syvänen, O. Nyrhilä, Characterization of process efficiency improvement in laser additive manufacturing, Phys. Procedia 56 (2014) 317–326, doi:10.1016/j.phpro.2014.08.177.
- [43] C. Ma, J. Zhao, C. Cao, T.C. Lin, X. Li, Fundamental study on laser interactions with nanoparticles-reinforced metals part I: effect of nanoparticles on optical reflectivity, specific heat, and thermal conductivity, J. Manuf. Sci. Eng. Trans. ASME 138 (2016) 121001, doi:10.1115/1.4033392.
- [44] C. Ma, J. Zhao, C. Cao, T. Lin, X. Li, Fundamental study on laser interactions with nanoparticles-reinforced metals-part II: effect of nanoparticles on surface tension, viscosity, and laser melting, J. Manuf. Sci. Eng. 138 (2016) 121002, doi:10.1115/1.4033446.
- [45] M. Qu, Q. Guo, L.I. Escano, A. Nabaa, S.M.H. Hojjatzadeh, Z.A. Young, L. Chen, Controlling process instability for defect lean metal additive manufacturing, Nat. Commun. 13 (2022) 1079, doi:10.1038/s41467-022-28649-2.
- [46] Q. Guo, M. Qu, L.I. Escano, S.M.H. Hojjatzadeh, Z. Young, K. Fezzaa, L. Chen, Revealing melt flow instabilities in laser powder bed fusion additive manufacturing of aluminum alloy via in-situ high-speed X-ray imaging, Int. J. Mach. Tools Manuf. (2022) 103861, doi:10.1016/j.ijmachtools.2022.103861.